Journal of Applied Microbiology, 2023, 135, 1–14
https://doi.org/10.1093/jambio/lxad309
Advance access publication date: 18 December 2023
Research Article

JOURNAL OF APPLIED MICROBIOLOGY
OXFORD UNIVERSITY PRESS

Effect of (in)organic additives on microbially induced calcium carbonate precipitation

Jamie Haystead[1], Katie Gilmour[1], Angela Sherry[1], Martyn Dade-Robertson[2,3], Meng Zhang[1,*]

[1]Hub for Biotechnology in the Built Environment, Department of Applied Sciences, Northumbria University, Ellison Place, Newcastle upon Tyne NE1 8ST, United Kingdom
[2]Hub for Biotechnology in the Built Environment, School of Architecture, Planning and Landscape, The Quadrangle, Newcastle University, Newcastle upon Tyne NE1 7RU, United Kingdom
[3]Hub for Biotechnology in the Built Environment, Department of Architecture and Built Environment, Northumbria University, NE1 8ST, United Kingdom

*Corresponding author. Hub for Biotechnology in the Built Environment, Department of Applied Sciences, Northumbria University, Ellison Place, Newcastle upon Tyne NE1 8ST, United Kingdom. E-mail: meng.zhang@northumbria.ac.uk

Abstract

Aim: This study aimed to understand the morphological effects of (in)organic additives on microbially induced calcium carbonate precipitation (MICP).

Methods and results: MICP was monitored in real time in the presence of (in)organic additives: bovine serum albumin (BSA), biofilm surface layer protein A (BslA), magnesium chloride ($MgCl_2$), and poly-L-lysine. This monitoring was carried out using confocal microscopy to observe the formation of $CaCO_3$ from the point of nucleation, in comparison to conditions without additives. Complementary methodologies, namely scanning electron microscopy, energy-dispersive X-ray spectroscopy and X-ray diffraction, were employed to assess the visual morphology, elemental composition, and crystalline structures of $CaCO_3$, respectively, following the crystals' formation. The results demonstrated that in the presence of additives, more $CaCO_3$ crystals were produced at 100 min compared to the reaction without additives. The inclusion of BslA resulted in larger crystals than reactions containing other additives, including $MgCl_2$. BSA induced a significant number of crystals from the early stages of the reaction (20 min) but did not have a substantial impact on crystal size compared to conditions without additives. All additives led to a higher content of calcite compared to vaterite after a 24-h reaction, with the exception of $MgCl_2$, which produced a substantial quantity of magnesium calcite.

Conclusions: The work demonstrates the effect of several (in)organic additives on MICP and sets the stage for further research to understand additive effects on MICP to achieve controlled $CaCO_3$ precipitation.

Impact Statement

The research findings are important for the development of controlled $CaCO_3$ bioproduction of different sizes and morphologies, which can have beneficial uses in a range of industrial applications.

Keywords: $CaCO_3$ morphology; (in)organic additives; microbially induced calcium carbonate precipitation (MICP); *Sporosarcina pasteurii*

Introduction

Calcium carbonate ($CaCO_3$) is an inorganic salt that occurs naturally in a variety of materials including chalk, limestone, and marble (Geyssant 2001). $CaCO_3$ is also present in marine organisms where it provides exoskeleton strength, protection from injury, or shelter (Wu et al. 2017). Additional occurrences of $CaCO_3$ in nature include teeth and bones of vertebrates (Mann 2001) and induced precipitation by bacteria (Dade-Robertson et al. 2015). $CaCO_3$ has a number of polymorphs. The crystalline polymorphs of $CaCO_3$ that are mainly observed are aragonite, calcite, and vaterite, each of which have characteristic morphologies, which are needle-like, rhombohedral, and spherical, respectively (Minkowicz et al. 2021). Other polymorphs consist of metastable hydrated forms of $CaCO_3$ such as monohydrocalcite, ikaite, and $CaCO_3$ hemihydrate (Clarà Saracho et al. 2021), as well as different phases of polymorphs, including the recently reported calcite-Vb (Druzhbin et al. 2022). Morphologies observed in marine organisms can be more complex due to the interaction of $CaCO_3$ with inorganic and organic compounds. Overall, the wide range of $CaCO_3$ presents the potential for controllable mineral synthesis for new types of material production (Dade-Robertson et al. 2015).

$CaCO_3$ can be found in extensive applications, with different polymorphs offering advantageous properties for specific uses. For example, aragonite has application in papermaking, calcite is utilized for drug delivery, and vaterite is incorporated into teeth whitening products. In addition, the sizes and formation rates of crystals are crucial factors in various applications, notably in the context of microbially induced calcium carbonate precipitation (MICP) for geoengineering purposes. For example, when $CaCO_3$ was used to stabilize soils, smaller crystals were found to give a higher unconfined compressive strength compared to larger crystal sizes (Putra et al. 2016). Furthermore, rate differences of crystal formation can be important for applications such as self-healing concrete, which would benefit from faster crystal formation (Zaerkabeh et al. 2022).

Received 7 October 2023; **revised** 28 November 2023; **accepted** 15 December 2023

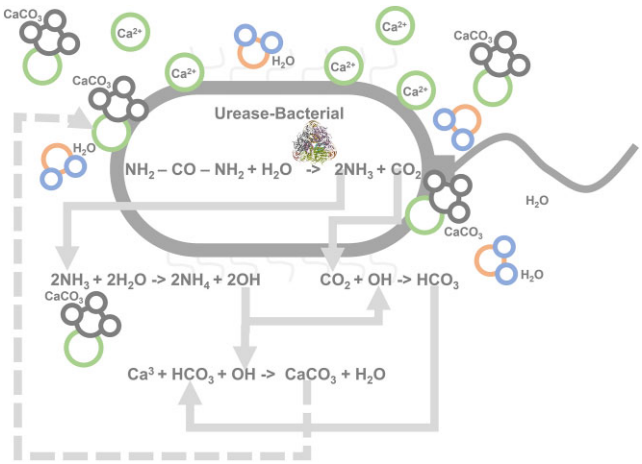

Figure 1. Schematic diagram of MICP through ureolytic bacteria.

Due to the diverse practical application of $CaCO_3$, its synthesis has been extensively carried out through chemical methods such as carbonation, hydrothermal and solvothermal synthesis, water-in-oil reverse emulsion routes, and ultrasonic intensification routes (Liendo et al. 2022, Niu et al. 2022). Over the last decade, industrial demands have driven the extensive research in the controlled synthesis of $CaCO_3$. Studies have demonstrated that different morphologies can be achieved by altering synthesis conditions such as reactant concentration (Bahrom et al. 2019).

More recently, MICP is seen as an alternative method to chemical production of $CaCO_3$ for use in various applications due to advantages in lower greenhouse gas production and production costs (Yi et al. 2021). Applications of MICP include bio-bricks (Yu and Rong 2022), dust suppression (Yu and Zhang 2023a), mortar crack repair (Yu and Zhang 2023b), slope stability (Xiao et al. 2022), and soil stabilization (Yu et al. 2022, 2023, Yu and Pan 2023). Bacterial cells and associated biological activities mediate the formation of $CaCO_3$. Most research focuses on the ureolytic pathway approach, which features the hydrolysis of urea to form ammonia (NH_3) and carbon dioxide (CO_2) (Fig. 1). The CO_2 forms carbonate (CO_3^{2-}) that can react with calcium (Ca^{2+}) in the local environment to form $CaCO_3$, whilst NH_3 forms an equilibrium with ammonium (NH_4^+) and causes a local pH rise, which creates favourable conditions for $CaCO_3$ formation and precipitates from solution when oversaturated. Bacterial cells can also act as nucleation sites for $CaCO_3$ formation by accumulating Ca^{2+} on the negatively charged cell walls, which promotes crystal formation on cell surfaces (Zhang et al. 2018).

There are numerous chemical synthesis studies that have been conducted to understand how to control $CaCO_3$ precipitation to achieve specific morphologies, and a comprehensive review has been conducted by Niu and colleagues (Niu et al. 2022). Yet few studies have explored the use of additives alongside MICP to modify $CaCO_3$ morphology and precipitation rate. The use of additives can have two main impacts on MICP, including altered the urease activity of the bacteria and the morphology of the formed $CaCO_3$. In the limited MICP studies conducted, the majority have investigated inorganic additives, e.g. magnesium chloride ($MgCl_2$), Na-montmorillonite and nickel chloride ($NiCl_2$). The most common additive investigated has been $MgCl_2$, which has been shown to promote acicular aragonite in place of rhombohedral calcite (Boyd 2012, Boyd et al. 2014, Putra et al. 2016, Xu et al. 2020). Na-montmorillonite was shown to provide nucleation sites for precipitation to occur and increase overall $CaCO_3$ precipitation, although at high concentrations, precipitation was elevated to a lesser extent. Na-montmorillonite caused $CaCO_3$ to change to an irregular rhombohedral morphology (Tang et al. 2021). Another additive that has been well studied is $NiCl_2$ that can increase ureolysis rate of bacteria by promoting higher urease content per cell, which has subsequent effects on $CaCO_3$ precipitation rate (van Paassen 2009, Connolly et al. 2013, Dhami et al. 2013, 2017, Rowshanbakht et al. 2016, Cheng et al. 2017). However, concentrations >500 μM $NiCl_2$ can have inhibitory effects on cell growth and $CaCO_3$ precipitation (Bachmeier et al. 2002). $NiCl_2$ has not been studied in detail for the effects on $CaCO_3$ morphology. Less studies have been conducted into the effect of organic additives on MICP. The poly amino acid, poly-L-lysine, has previously been shown to promote the formation of ellipsoidal-shaped aggregates in place of rhombohedral calcite (Nawarathna et al. 2018a, b). Whereas, nonfat milk powder has been used during enzyme-induced $CaCO_3$ precipitation, which can aggregate Ca^{2+} together and act as nucleation sites, as well as delay precipitation due to a chelating effect from casein (Almajed et al. 2019). In addition to individual additives, there is evidence that bacterial extracellular polymeric substances (EPS) have an impact on $CaCO_3$ nucleation and morphology, although due to the variations in EPS composition that can occur, this can both promote and inhibit $CaCO_3$ precipitation (Decho and Gutierrez 2017). The goals of this work were to determine the effects of several additives on MICP, with a focus on understanding the process of crystal formation from the start to the end point of $CaCO_3$ precipitation.

Materials and methods

Bacterial culture conditions

Sporosarcina pasteurii strain DSM 33 was used for all experiments (Yoon et al. 2001). Cultures were grown in nutrient media containing nutrient broth (13 g l^{-1}), with 187 mM NH_4Cl and 333 mM urea at 30°C, 150 RPM to early stationary phase. Harvested cultures were washed three times in phosphate-buffered saline (NaCl 136.89, KCl 2.68, Na_2HPO_4 8.95, and KH_2PO_4 1.76 mM, pH 7.4) with centrifugation at 18 516 × *g* for 15 min, 4°C, (Universal 320, Hettich, Germany). Following washing, cells were resuspended in 18.2 MΩ cm H_2O to the optical density at a wavelength of 600 nm (OD600nm) of 2.8, which is equivalent to ~8.27×10^8 cells ml^{-1}; based on an *S. pasteurii* OD/cell number conversion of 2.95×10^8 per OD_{600nm} (Haystead 2023). Cultures were stored on ice until required for experimental work. Additional tests were performed using cells 5 h after the wash step. Cultures were removed from ice 5 min prior to use in experiments to allow to reach room temperature. The ureolysis activity of *S. pasteurii* has been measured in our previous study through a conductivity assay adapted from existing literature (Van Passen 2009and Whiffin 2004). Under the same conditions, it was shown that the *S. pasteurii* whole cells have an activity of 22.05 mM OD_{600nm}^{-1} min^{-1} (Haystead 2023).

Real-time observation of crystal formation in response to additives

Several different additives were selected for testing to determine the effects on $CaCO_3$ crystal formation from MICP.

Bovine serum albumin (BSA) is a protein extracted from cow plasma, which consists of 583 amino acids (Hirayama et al. 1990). Other researchers have shown that BSA has adhesive properties and may potentially function as a binder (Roberts et al. 2020, 2021). The biofilm surface layer protein A (BslA) is a common biofilm hydrophobin protein, which is able to self-assemble at interfaces to provide a hydrophobic coating of surfaces (Hobley et al. 2013), and features a large hydrophilic domain with a small hydrophobic cap (Ramos et al. 2022). BslA has not yet been studied alongside $CaCO_3$ precipitation, yet is hypothesized to have an impact on $CaCO_3$ precipitation based on interactions of other globular protein-charged residues on $CaCO_3$ precipitation (Robles-Fernández et al. 2022). $MgCl_2$ has been studied in a variety of MICP studies, although there is a research gap of studying $CaCO_3$ precipitation in real time. The final additive selected for study was poly-L-lysine because it has been demonstrated previously that charged polypeptides can have an impact on $CaCO_3$ crystal formation (Nawarathna et al. 2018a, b), which is important to study due to the presence of polypeptides in bacterial EPS (Huang et al. 2022). Nawarathna et al. (2018a) have previously studied poly-L-lysine effects on MICP, although not with *S. pasteurii*, therefore, this seemed an ideal polypeptide to test to add to this body of knowledge.

MICP reaction mixtures included nutrient broth (3 g l^{-1}), with 500 mM $CaCl_2$, 187 mM NH_4Cl, and 500 mM urea, which were additive-free baseline conditions to which reaction mixtures containing additives were compared. In addition to this, additives were investigated separately, and the concentrations used for these additives are BSA at 75 mg l^{-1}, BslA at 400 mg l^{-1}, $MgCl_2$ at 125 mM, and poly-L-lysine at 100 mg l^{-1}. Cells were added as a final step to start MICP reactions 30 min after being washed to a working concentration of 4.13×10^8 CFU ml^{-1}. Two negative controls were set up, which were the same as the baseline conditions where one control was acellular and one control contained no urea. Confocal laser scanning microscopy (DMi8, Leica Microsystems) was used to visualize a 50 µl drop from each reaction mixture using bright-field mode with images taken using the wide-field image acquisition function at time intervals of 0, 20, 40, 60, 80, and 100 min. Image view fields were 150 × 110 µm and at least three images were captured per time point under all conditions. Additionally, to monitor formation of MICP from nucleation in real time, each condition was monitored at a fixed position using time lapse at 1-min intervals over a 120-min period. Experiments were performed at room temperature (20°C–22°C). Three biological replicates were performed for each condition.

Quantification of crystal formation: size and total crystal number

Images captured using confocal microscopy were assessed for total crystal number and crystal diameter measurements in FIJI (version 2.9.0). For each time point, condition and biological replicate, three images were selected for analysis. Measurements of crystals (µm) in images analysed for each time point and condition were averaged and standard error was calculated. For tests where cells were used 5 h after the wash step, only 100-min time points were assessed and for each image, 25 crystals were selected for size measurement. Either a one-way ANOVA or Kruskal–Wallis ANOVA test was used for statistical analysis of total crystal number and crystal diameter measurements and was performed in IBM SPSS (version 28.0.0.0). A Kolmogorov–Smirnov test was used to assess if variables were normally distributed before selecting the statistical test. Either Student–Newman–Keuls (SNK) or Tamhane's T2 *post hoc* statistical analysis was used alongside one-way ANOVA tests depending on homogeneity of variances.

pH monitoring during crystal formation in real-time

MICP reactions were set up in the same manner as for confocal microscopy experiments, using a volume of 10 ml. Reactions were performed at room temperature (20°C–22°C) and the pH was measured (Accumet AE150 Benchtop pH Meter, Fisher Scientific) at 0, 20, 40, 60, 80, and 100 min, as well as after 24 h. Three biological replicates were performed for each condition.

Morphology and elemental composition analysis

MICP reactions were set up in the same manner as the confocal microscopy experiments, using a volume of 50 ml. Samples were kept at room temperature (20°C–22°C) for 24 h. Precipitated $CaCO_3$ was collected by passing samples through filter paper (0.2 µm) and washing three times with distilled H_2O. Samples were dried at 70°C for 24 h then stored in a desiccator for a further 24 h.

To assess visual morphology Scanning Electron Microscope (SEM) and elemental composition Energy-Dispersive X-ray Spectroscopy (EDS), precipitated $CaCO_3$ from each reaction mix was applied to carbon discs on 12 mm aluminium stubs. The sample top surface was coated in 4 nm chromium using a sputtering machine (Q150T ES Plus, Quorum Technologies). Samples were visualized on an SEM at 3 kV to minimize sample damage with associated software (TESCAN MIRA3, Czech Republic). EDS analysis was performed at 20 kV in triplicate with AZtecLive 6.1 software (Oxford Instruments).

Structural properties analysis

Precipitated $CaCO_3$ was crushed using a pestle and mortar and packed into XRD sample holders. XRD data were collected using a Rigaku SmartLab diffractometer with Cu Kα radiation (40 kV and 50 mA) using SmartLab Studio II software. Measurement parameters were 0.01° 2θ step size, 2 s per step and 5–65° 2θ exploration range. XRD samples were identified and quantified using HighScore Plus software. XRD chromatograms were integrated to determine peak profiles for each reaction mix. Peak profiles were subsequently compared to the crystallography open data (COD) database to provide a structural match and crystalline phase identification of the data for ammonium chloride (COD ID 96-900-7494), calcite (COD ID 96-901-5391), magnesium calcite (COD ID 96-721-4218), and vaterite (COD ID 96-900-7476).

Results

$CaCO_3$ crystal morphology changes in response to additives

Under confocal microscopy, $CaCO_3$ crystal formation started to occur from 20 min under most conditions tested in this study. However, morphological differences were most clearly observed at 100 min, therefore, images were compared at this time point (Fig. 2). Additive-free conditions showed a mixture of calcite crystals and spherical vaterite (Fig. 2a–c). Crystal formation for this condition at 20, 40, 60, 80, and

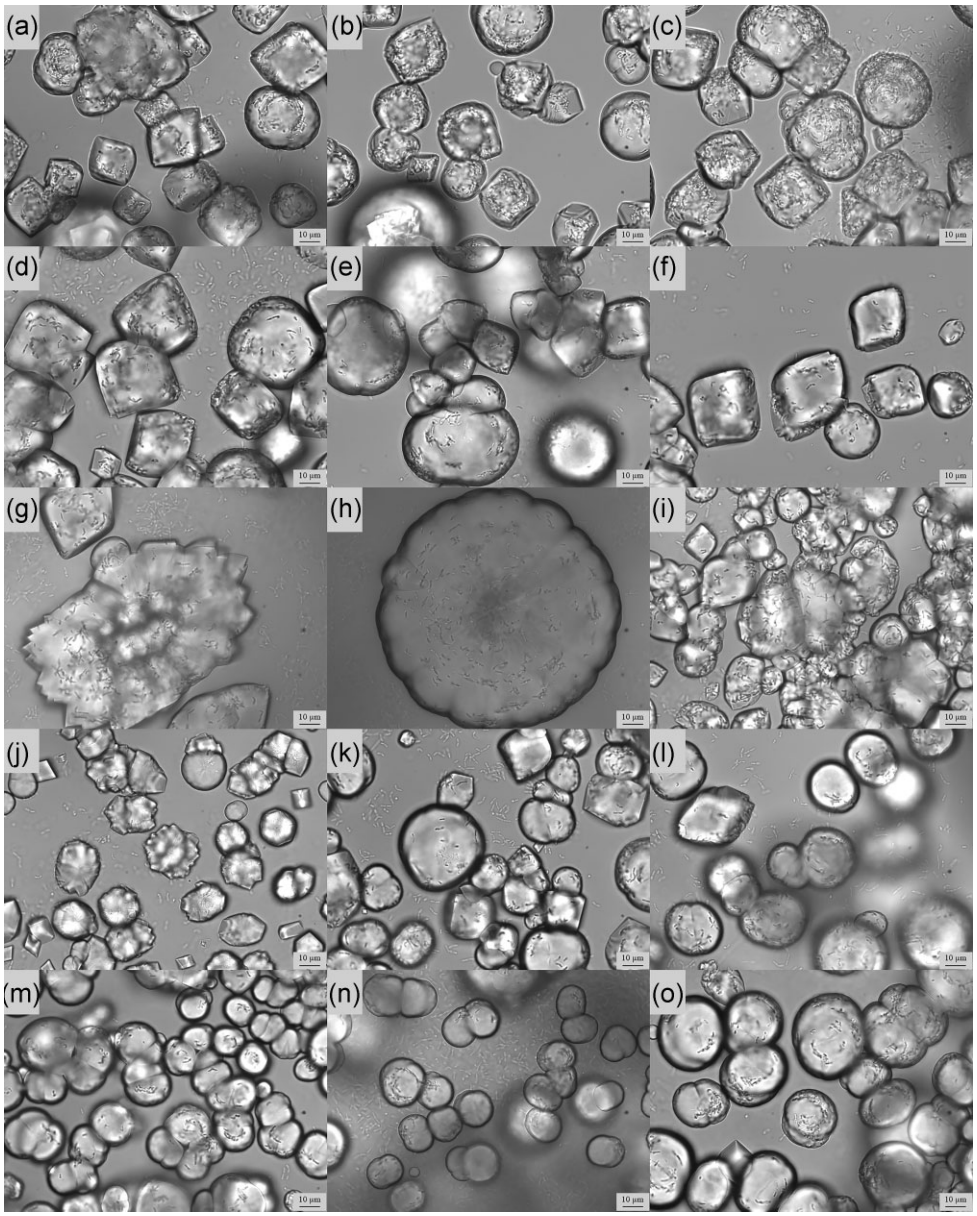

Figure 2. $CaCO_3$ formations observed during confocal microscopy experiments after 100 min under all conditions. (a–c) Additive-free conditions, (d–f) BSA additive conditions, (g–i) BslA additive conditions, (j–l) $MgCl_2$ additive conditions, and (m–o) poly-L-lysine additive conditions.

100 min showed the initial overall $CaCO_3$ morphology was vaterite, which started to transform to calcite from 80 min (Supplementary Fig. S1). Additive-free conditions compared to acellular and urea-free negative controls at 100 min confirmed that observed $CaCO_3$ structures were caused by MICP (Supplementary Fig. S2). BSA additive produced $CaCO_3$ crystals of similar morphology distribution compared to additive-free conditions (Fig. 2d–f). Addition of the hydrophobic protein BslA produced unique $CaCO_3$ formations that were not observed under additive-free or BSA conditions, which included jagged structures (Fig. 2g), large spherical structures (Fig. 2h), as well as calcite and vaterite as observed under previous conditions (Fig. 2i). $MgCl_2$ as an additive showed the presence of jagged $CaCO_3$ morphologies (Fig. 2j) in addition to calcite and vaterite (Fig. 2k and l), although the jagged morphologies were smaller compared to those formed with BslA as an additive (compare Fig. 2j to g). Inclusion of poly-L-lysine resulted in mainly spherical vaterite formations occurring of similar size to additive-free conditions, with minimal calcite observed (Fig. 2m–o).

Due to the unique nature of crystal formation when BslA was present as an additive (Fig. 2g–i), $CaCO_3$ morphologies were investigated in more detail across the time series (Fig. 3). The early stages of the unique formations can be observed at 60 min and feature a perimeter of $CaCO_3$ (Fig. 3a–c). The $CaCO_3$ perimeters then fill with $CaCO_3$ as well as expand to form floral/jagged structures, which are observed at 80 (Fig. 3d–f) and 100 min (Fig. 3g–i).

$CaCO_3$ crystal measurements in response to additives

The number of individual crystals under additive-free conditions peaked at 60 min with 36.44 ± 3.56, then declined until 100 min with 17.89 ± 8.06 (Fig. 4a). All additives

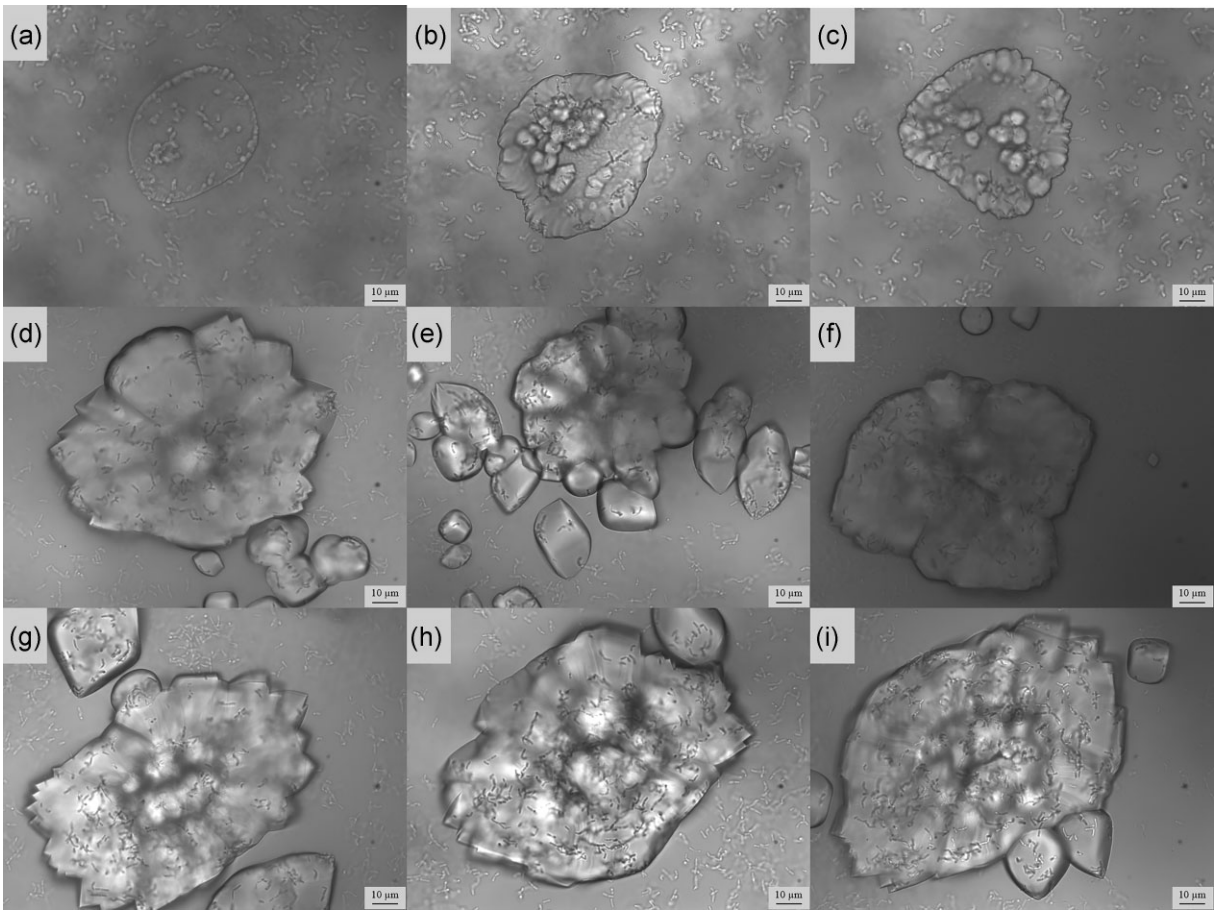

Figure 3. $CaCO_3$ formations observed during confocal microscopy experiments for BslA additive at different time points showing the formation process of unique $CaCO_3$ morphologies at 60 (a–c), 80 (d–f), and 100 min (g–i).

investigated produced a higher number of crystals by 100 min compared to additive-free conditions, which were 34.22 ± 9.24, 23.44 ± 13.78, 21.11 ± 8.79, and 39.56 ± 5.47 for BSA, BslA, $MgCl_2$, and poly-L-lysine, respectively. BSA crystal numbers peaked at 40 min with 73.78 ± 4.69 crystals, which declined until 100 min, BslA crystal numbers peaked at 100 min with 23.44 ± 13.78 crystals, $MgCl_2$ crystal numbers peaked at 80 min with 22.00 ± 10.07 crystals with a small decrease at 100 min, and poly-L-lysine crystal numbers also peaked at 80 min with 47.89 ± 28.43 crystals with a small decrease at 100 min. Treatments containing BSA generated significantly higher crystal numbers than treatments with other additives at 40 min ($P = .002$ with sample groupings confirmed by SNK analysis), and by 60 min significantly higher crystal numbers continued to be produced with BSA additive in comparison to $MgCl_2$ and poly-L-lysine additives ($P = .012$ with samples groupings confirmed by SNK analysis). Significant differences in crystal number between additive amended reactions were not apparent at later time points ($P > .05$).

Crystal measurements at 100 min under additive-free conditions showed an average diameter of 33.26 ± 9.70 μm (Fig. 4b). BSA, $MgCl_2$, and poly-L-lysine produced smaller crystals at 100 min of sizes 20.88 ± 1.76, 21.51 ± 3.25, and 18.55 ± 1.05 μm, respectively, whilst BslA produced larger crystals of 45.48 ± 15.63 μm. There were no significant differences in crystal size under conditions containing additives in comparison to additive-free conditions at any time point ($P > .05$).

pH changes of MICP reactions in response to additives

There were no significant changes in pH observed in all the experiments performed during this study. Initial pH at 0 min under additive-free, BSA, and BslA conditions were 7.69, 7.70, and 7.73, respectively, whilst the pH for $MgCl_2$ and poly-L-lysine conditions was slightly lower at 7.35 and 7.40, respectively. Following this, pH under all conditions varied within the neutral range of 7.58–8.01 over the monitored 24 h. The maximum standard error recorded was 0.01.

$CaCO_3$ morphology, structural, and elemental composition after 24 h

Further morphology, structural, and elemental analysis demonstrated most of the conditions tested in this study produced a higher content of calcite compared to vaterite. $CaCO_3$ visualization under additive-free conditions after 24 h of formation showed hollow spherical structures of $CaCO_3$ as well as layered $CaCO_3$ formations (Fig. 5a). The content of calcite was 78.8% and vaterite was 21.2%. BSA additive conditions showed layered $CaCO_3$ formations and were absent of spherical formations (Fig. 5b). Majority (90.1%) of those are calcite with only 9.9% vaterite. BslA additive conditions

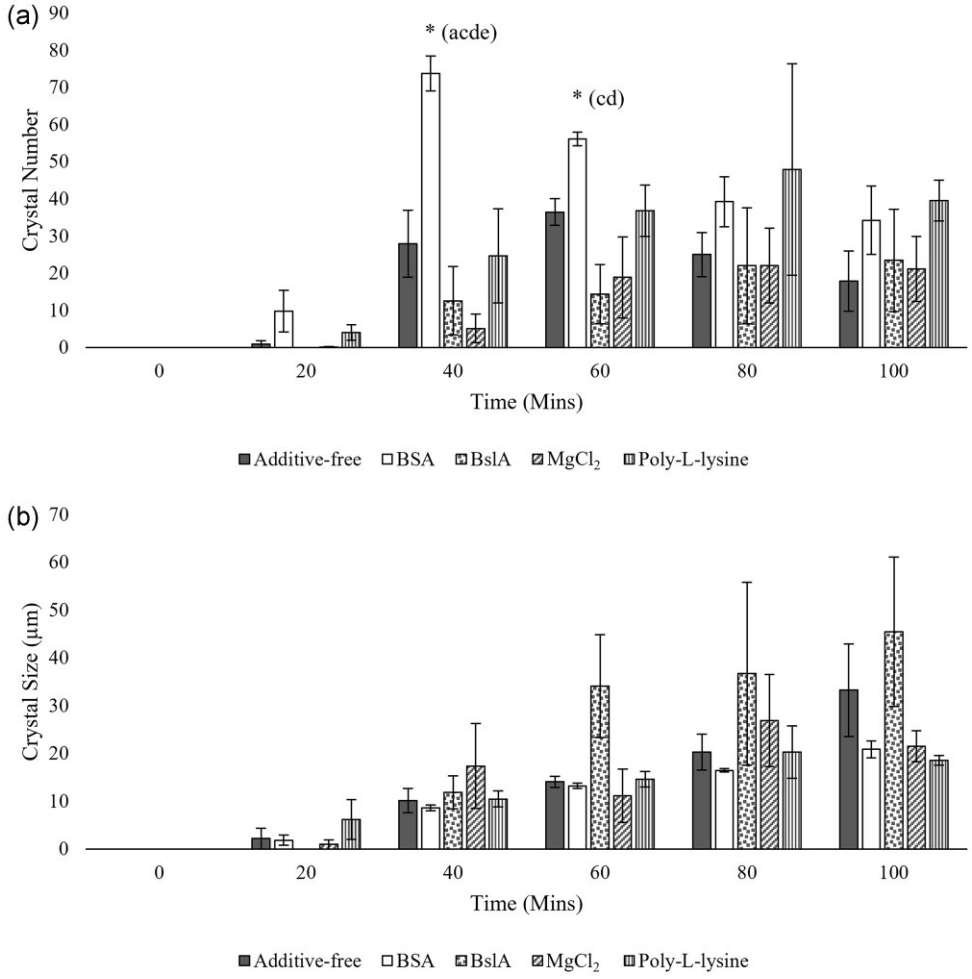

Figure 4. $CaCO_3$ crystal measurements at 0, 20, 40, 60, and 100 min under all conditions. (a) Average crystal numbers. (b) Average crystal size. All measurements were counted within 150 × 110 μm view fields and were the average of three biological replicates, with three technical replicates conducted per biological replicate. Error bars show standard error. * show significant differences at $P < .05$.

showed small hollow spherical $CaCO_3$ formations similar to additive-free conditions along with layered $CaCO_3$,with a lower proportion of spherical $CaCO_3$ (Fig. 5c). They constitute 88.5% calcite and 11.5% vaterite. Interestingly, $MgCl_2$ additive conditions showed high amounts of layered $CaCO_3$ formations and were absent of spherical formations, similar to BSA (Fig. 5d). The content of calcite was 45.3% and magnesium calcite was 54.7%, with no detection of vaterite. Poly-L-lysine additive conditions showed much larger spherical $CaCO_3$ structures, which were not hollow, with low amounts of layered $CaCO_3$ formations (Fig. 5e). The content of calcite was 90.1% and vaterite was 9.9%. Overall, the morphology of additive condition crystals featured fewer spherical $CaCO_3$ and high amounts of large layered $CaCO_3$ structures apart from poly-L-lysine, which still displayed high proportions of spherical $CaCO_3$. EDS of additive-free, BSA, BslA, and poly-L-lysine conditions confirmed that all structures detected were $CaCO_3$, and conditions containing $MgCl_2$ contained the elements carbon, calcium, magnesium, and oxygen in the expected proportions (Fig. 5). The content of Mg^{2+} was 2.5%–8.3% in analysed sections of triplicate samples. A comparison of the ratios of $CaCO_3$ polymorphs highlighted differences between additive-free and additive-amended conditions (Fig. 5f).

$CaCO_3$ formation in cells 5 h after washing and dendrite formation

In addition to investigating the impact of the additives on MICP, cell metabolism also appeared to affect the process in terms of the crystal precipitation rate and size. These were observed by confocal analysis when the reaction contained cells 5 h after washing (Fig. 6), which demonstrated significantly higher $CaCO_3$ precipitation at 100 min compared to the same time point using cells 30 min after washing shown in Fig. 2. Due to the high volume of crystals, crystal numbers were not quantified and only 25 crystals per image were measured for crystal dimensions. Overall, crystals for all samples were smaller in size (Fig. 7). Assessment of $CaCO_3$ at earlier time points for cells used 5 h after washing showed similar $CaCO_3$ morphologies, sizes, and crystal numbers to occur at 20 min under BSA additive conditions, 40 min under additive-free conditions, BslA additive conditions, and poly-L-lysine additive conditions, and 60 min under $MgCl_2$ additive conditions (Supplementary Fig. S3). However, $CaCO_3$ at these time points were not identical to cells used 30 min after washing samples. The main differences were smaller crystals and higher crystal numbers, higher vaterite morphologies for BSA, and higher calcite morphologies for poly-L-lysine.

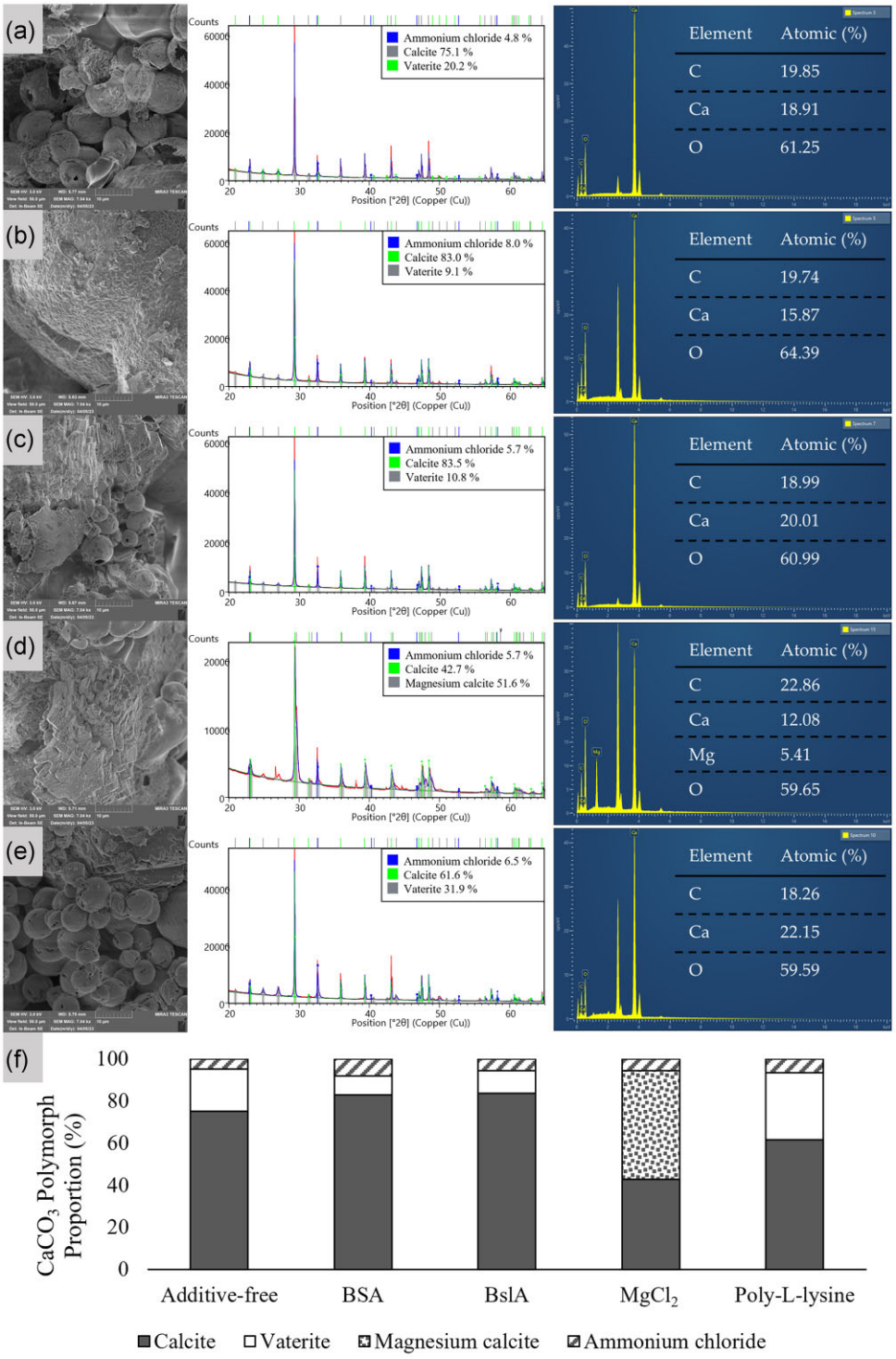

Figure 5. $CaCO_3$ analysis by SEM, XRD, and EDS of samples after 24 h under all conditions. (a) Additive-free conditions, (b) BSA additive conditions, (c) BslA additive conditions, (d) $MgCl_2$ additive conditions, (e) poly-L-lysine additive conditions, and (f) stacked bar chart of calcite polymorph ratios under all additive conditions, assessed by XRD of samples after 24 h.

Dendrite formation was observed and documented at the 120-min time point and was observed in both sets of test samples and negative controls (Supplementary Fig. S4). Videos were also captured to evidence this (Videos S3, S4, and S5). Dendrite formation obstructed the field of view and made it unfeasible to observe or measure other $CaCO_3$ formations.

Discussion

$CaCO_3$ crystal formation in real time

The utilization of confocal microscopy revealed the precipitation of $CaCO_3$ over time and the impact of additives on growth and morphology of the crystals (Fig. 2). Initially, under additive-free conditions, the observed morphologies were

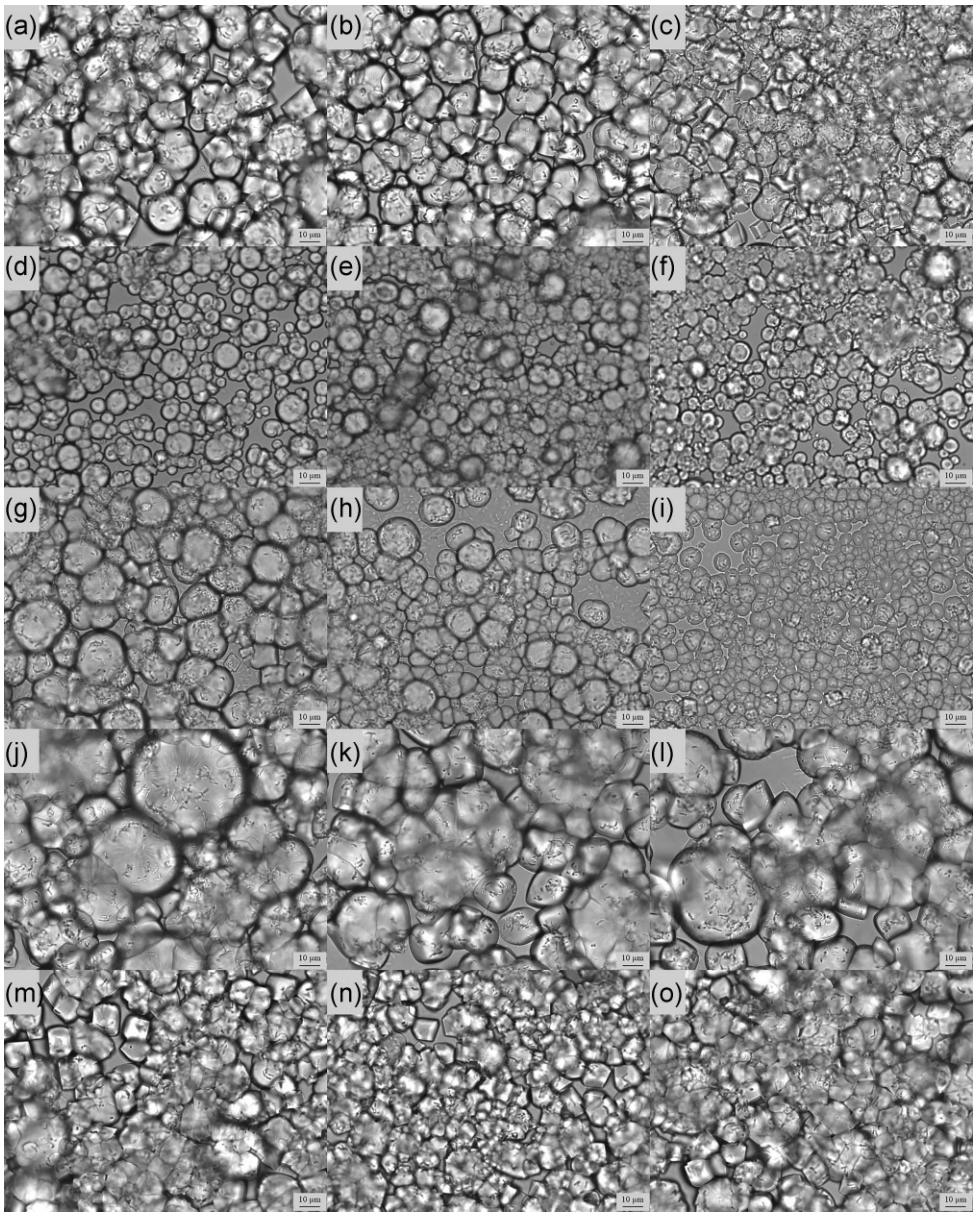

Figure 6. $CaCO_3$ formations observed during confocal microscopy experiments after 100 min under all conditions using cells 5 h following the washing step instead of 30 min following the washing step. (a–c) Additive-free conditions, (d–f) BSA additive conditions, (g–i) BslA additive conditions, (j–l) $MgCl_2$ additive conditions, and (m–o) poly-L-lysine additive conditions.

spherical, which is indicative of vaterite and represents the most common vaterite morphology (Udrea et al. 2012). Over time, the vaterite formations increased in size indicating nucleation of $CaCO_3$ on pre-existing $CaCO_3$ formations (Fig. 4b); however, individual crystal numbers decreased by 100 min showing that either crystals merged together when in close proximity or that the growth of larger crystals obstructed existing crystals from the field of view (Fig. 4a). By 100 min, the additive-free conditions showed a mixture of rhombohedral calcite crystals and spherical vaterite (Fig. 2a–c), demonstrating transformation of a proportion of the vaterite to calcite, which is thermodynamically more stable. The presence of vaterite polymorphs can still be observed due to stabilization by ammonium (Hu et al. 2012), which prevents transformation to calcite by interaction with CO_3^{2-}. Literature shows that higher proportions of vaterite are formed at pH <8 (Chen et al. 1997, Chang et al. 2017), which aligns with the initial pH of the reaction solution (pH 7.69). Overall, pH changes were minor over the 100 min and were not the cause of crystal transformation from vaterite to calcite. Other studies have shown using chemical precipitation tests at 24°C that pure vaterite forms below pH 10 and pure calcite forms at pH 11 (Gómez-Morales et al. 1996a, b). However, it should be noted that multiple factors influence $CaCO_3$ morphology, including temperature and the presence of additive (Boulos et al. 2014), and the optimum pH range may vary under different conditions. After 24 h, XRD detected a mixture of calcite and vaterite, which were observed as layered $CaCO_3$ and hollow spherical $CaCO_3$, respectively (Fig. 5a). This demonstrated that $CaCO_3$ morphologies observed in real time from nucleation remained stable following complete crystal formation. Size similarities of spherical crystals between 100 min

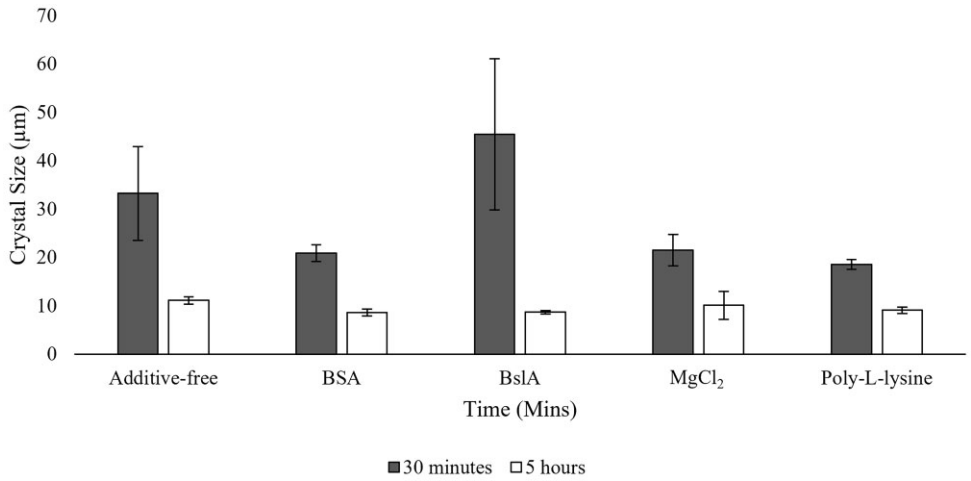

Figure 7. Comparison of $CaCO_3$ crystal measurements at 100 min under all conditions for cells that were used 30 min after the wash step and cells that were used 5 h after the wash step. All measurements were counted within 150 × 110 µm view fields and were the average of three biological replicates, with three technical replicates conducted per biological replicate. Error bars show standard error.

and 24-h time points suggested that under the current testing conditions, the size of crystals does not significantly grow beyond 100 min, although new crystal nucleation may still occur after 100 min. pH increases were minor after 24 h and would have had minimal impact on $CaCO_3$ morphologies formed.

$CaCO_3$ crystal formation in real time in response to additives

Whilst there were no significant morphological differences between BSA additive and additive-free conditions (Fig. 2d–f compared to Fig. 2a–c), there were a higher number of smaller crystals (Fig. 4). This could occur due to more nucleation sites, which are provided by charged residues of BSA, which consists of 17.2% polar and acidic amino acids and 17.0% polar and basic amino acids (Hirayama et al. 1990). Electrostatic interactions from BSA incorporated into $CaCO_3$ may have an inhibitory effect on crystal growth, causing $CaCO_3$ in solution to form new crystals as opposed to adding to existing crystals, as was observed in a study, which looked at the influence of synthetic, charged polypeptides on $CaCO_3$ polymorphs (Džakula et al. 2011). Monitored pH changes were similar to additive-free conditions, therefore, pH was not impacted by the presence of BSA. Higher calcite content was observed and measured after 24 h (Fig. 5b), showing that BSA can promote calcite formation.

Interestingly, hydrophobic protein BslA additive produced unique $CaCO_3$ formations that were not observed under additive-free conditions (Fig. 3). These structures could have occurred due to the hydrophobic properties of BslA (Morris et al. 2017). BslA may have self-assembled into a circular perimeter, which provides a scaffold for $CaCO_3$ nucleation (Fig. 3a–c). Following growth of $CaCO_3$ on the BslA perimeter, $CaCO_3$ growth occurs inside the perimeter until the structure is filled with $CaCO_3$ (Fig. 3d–i). In addition to the unique crystal morphologies, calcite and vaterite were present at similar distributions and sizes compared to additive-free conditions (Fig. 2g–i compared to Fig. 2a–c). Overall, crystals formed in similar numbers to additive-free conditions but were larger in size, showing that BslA can promote nucleation of $CaCO_3$ on existing crystals (Fig. 4). Before 80 min, crystal numbers were lower than additive-free conditions but larger in size, further evidencing that BslA promotes nucleation of $CaCO_3$ on existing crystals. Monitored pH changes remained in line with additive-free conditions, therefore, pH was not impacted by the presence of BslA. After 24 h, calcite content was higher, similar to BSA conditions; however, unique $CaCO_3$ morphologies were not observed at this stage (Fig. 5C). The layered $CaCO_3$ could be linked to the formation of floral/jagged structures, which promote growth of existing $CaCO_3$ crystals to larger sizes.

Addition of $MgCl_2$ showed similar jagged $CaCO_3$ structures observed under BslA conditions; however, these were of smaller size (Fig. 2j–l compared to Fig. 2a–c). Mg^{2+} may bind to early stage $CaCO_3$ formations and will inhibit growth of $CaCO_3$ by competition with Ca^{2+} for binding to CO_3^{2-} (Ahn et al. 2000). This inhibition will result in different areas of the $CaCO_3$ to grow at different rates, resulting in non-homogenous formations leading to jagged structures. Additionally, $CaCO_3$ precipitation rate was delayed when compared to additive-free conditions (Fig. 4a). By 80 min, similar numbers of crystals have formed compared to additive-free conditions, although crystal growth stagnates leading to higher $CaCO_3$ precipitation under additive-free conditions by 100 min (Fig. 4b). The delay occurred due to binding of Mg^{2+} with CO_3^{2-}, which is gradually substituted with Ca^{2+} to form $CaCO_3$ (Boyd 2012). Delayed precipitation by Mg^{2+} has been reported by a range of other studies (Boyd 2012, Boyd et al. 2014, Abdel Gawwad et al. 2016, Putra et al. 2016, Lv et al. 2022). Initial solution pH was 0.34 lower compared to additive-free conditions, which increases in line under additive-free conditions by 20 min. The initially lower pH as well as subsequent pH changes were similarly observed with poly-L-lysine conditions. No delay in $CaCO_3$ precipitation occurred with poly-L-lysine conditions, therefore, this indicates that pH was not a significant cause of $MgCl_2$ delayed precipitation under the conditions set up for this study. Furthermore, due to pH values increasing in line under additive-free conditions within 20 min, this shows that MICP processes can have a significant effect on the overall solution pH within a short time period. After 24 h, only calcite and magnesium calcite were observed and detected (Fig. 5d), showing that vaterite transforms to calcite in the presence of magnesium

chloride additive. Another study investigating the impact of Mg^{2+} in $CaCO_3$ crystal growth from sea water concluded that calcite containing greater than 8.5% molar content of $MgCO_3$ is less stable than aragonite (Berner 1975). This study detected a content of 54.7%, therefore, inclusion of $MgCl_2$ as an additive may not be suitable if $CaCO_3$ polymorph stability is important. Berner (1975) also observed that Mg^{2+} can retard the rate of $CaCO_3$ crystal growth due to incorporation of Mg^{2+} with the growing crystal, which is in agreement with crystal size measurements (Fig. 4b) and XRD data (Fig. 5d). Similar to BslA, $MgCl_2$ may promote the growth of existing $CaCO_3$ due to the presence of layered $CaCO_3$; however, this effect is not observed during the first 100 min due to the delayed precipitation effect by $MgCl_2$. Although aragonite is another polymorph of $CaCO_3$ that can form, especially in the presence of $MgCl_2$ (Putra et al. 2016), the conditions used during this work did not favour aragonite formation. Other factors that promote aragonite formation include a pH >12 (Gómez-Morales et al. 1996a, b), temperatures >40°C (Yasushi 1962), and low levels of $CaCO_3$ saturation (Somani et al. 2006). The temperature used for these experiments was 20°C–22°C, which does not favour aragonite formation. Although high pH promotes aragonite formation, high aragonite formation has been reported at a lower pH of 8.1 (Ahn et al. 2000). However, this was still higher than the pH measured during this study. Furthermore, the temperatures used by Ahn et al. (2000) were 80°C, which differs significantly to this study.

Inclusion of poly-L-lysine resulted in mainly spherical amorphous $CaCO_3$/vaterite formations occurring of similar size to additive-free conditions, with minimal calcite observed (Fig. 2m–o compared to Fig. 2a–c). By 100 min, total crystal numbers were higher than additive-free conditions and were smaller in size, similar to BSA, which demonstrates the ability of poly-L-lysine to promote nucleation of new crystals (Fig. 4). Initial pH was lower than additive-free conditions but increased in line under additive-free conditions by 20 min similar to $MgCl_2$ conditions, which provides further evidence that MICP processes can significantly influence solution pH within a short time period. Structural analysis after 24 h measured higher calcite and lower vaterite compared to additive-free conditions, although the morphology of $CaCO_3$ remained largely spherical (Fig. 5e). These spherical structures appeared solid compared to the hollow crystals under additive-free conditions. MICP studies by Nawarathna et al. also investigated the use of poly-L-lysine on $CaCO_3$ morphology; however, a key difference with these studies was the use of *Pararhodobacter* sp. instead of *S. pasteurii* (Nawarathna et al. 2018a, b). The main morphologies observed were calcite, which is in agreement with XRD measurements, although observed morphologies in this study were spherical, which is not characteristic of calcite. Nawarathna et al. (2018b) found from Fourier-transform infrared spectroscopy analysis that poly-L-lysine was incorporated into $CaCO_3$ crystals and may provide nucleation sites, which can account for differences in morphology. In the case of these experiments, incorporation of poly-L-lysine to $CaCO_3$ crystals may help to stabilize the spherical $CaCO_3$ structures, although doesn't prevent calcite formation due to calcite detection by XRD. Higher concentrations of poly-L-lysine may minimize calcite formation. There is evidence of poly-L-lysine acting as nucleation sites too as demonstrated through higher crystal numbers observed in our study.

Additional observations

Impact of cell metabolism on crystal formation

$CaCO_3$ nucleation occurred faster and at higher quantities when using cells 5 h after washing compared to 30 min after washing (Fig. 6 compared to Fig. 2). Comparable $CaCO_3$ occurred at much earlier time points for all samples using cells 5 h after washing, although crystals were overall smaller and at higher quantities than when using cells 30 min after washing (Supplementary Fig. S3 compared to Fig. 2). An explanation for this is that after *S. pasteurii* was washed, there were still ureolysis products within the cells such as CO_3^{2-} and NH_4^+. These products are able to diffuse freely into the surrounding medium (Wiley and Stokes 1963), therefore, these products diffused over time into the H_2O used for bacterial resuspension. Potentially, urea in the original culture medium could have diffused into cells prior to washing, which would be hydrolyzed by urease during or after the wash step. Washed bacterial culture after 5 h will contain increased concentrations of these ions due to a longer period of diffusion compared to 30 min, therefore, this may have promoted higher rates of $CaCO_3$ precipitation for these time points. Despite storage of cells on ice before starting MICP reactions, other cell metabolic processes may also contribute to higher concentrations of CO_3^{2-} for cells utilized 5 h after washing. For example, menaquinone (vitamin K2) biosynthesis (Jiang et al. 2007) and synthesis of branched chain amino acids (Chipman et al. 1998) can both produce CO_2 in *S. pasteurii*, which will lead to higher CO_3^{2-} concentrations. Overall, increased $CaCO_3$ precipitation may have occurred due to both higher diffusion of ureolysis reaction products out of cells into the bacterial resuspension medium and cell metabolic processes that produce CO_2. Additionally, crystal sizes were smaller under all conditions at 100 min with 5 h postwash samples compared to 30 min postwash samples (Fig. 7). These findings align with other works that demonstrated faster $CaCO_3$ precipitation rates and high degrees of supersaturation resulting in smaller $CaCO_3$ crystals (Liendo et al. 2022). It is further confirmed that $CaCO_3$ crystal size could be controlled by using bacteria with different urease expression levels. For example, *Escherichia coli* engineered with urease cassettes of different activity levels showed a relationship between urease expression and $CaCO_3$ size, with larger crystals forming at lower expression levels (Liang et al. 2018). Finally, differences in crystal polymorph were observed when comparing $CaCO_3$ using cells 5 h after washing to 30 min after washing (Supplementary Fig. S3 compared to Fig. 2). These include higher vaterite content under BSA additive conditions and higher calcite content with poly-L-lysine addition. This evidences that cell metabolism has an impact on $CaCO_3$ morphology as well as size and crystal number, which highlights the importance for controlling urease expression and the contents of the cell resuspension medium to achieve predictable $CaCO_3$ precipitation.

Nucleation and growth of $CaCO_3$ crystals in MICP

From the literature, there are numerous reports determined from indirect SEM imaging of *S. pasteurii* acting as nucleation sites for $CaCO_3$ precipitation to occur (Bang et al. 2010, Achal and Pan 2014, Xu et al. 2015, Fu et al. 2023), and this is considered an important role of the cells for the formation of $CaCO_3$ in addition to facilitating MICP reactions. However, when monitoring formation of $CaCO_3$ from collected images (Fig. 2) and time lapse (Videos S1 and S2), it

was not clear whether *S. pasteurii* were required for the initial nucleation of $CaCO_3$. Firstly, for many $CaCO_3$ formations, the cells were not required as nucleation sites as there were no bacteria embedded in the central region. If cells initiated the precipitation, the observation of *S. pasteurii* cells within the centre of all $CaCO_3$ formations would be expected. Secondly, $CaCO_3$ formations were observed to grow over time, whilst the number of new $CaCO_3$ formations occurred at a low rate, which showed that newly formed $CaCO_3$ had a preference for nucleating on existing $CaCO_3$ instead of nucleating from free bacteria. A number of $CaCO_3$ free bacteria can be observed in the medium at 100 minutes, therefore, there was not an issue of there being no available bacteria cells for $CaCO_3$ precipitation to occur on (Fig. 2). Similar observations were made during experiments featuring physical barriers between bacteria and the reaction solution to give bacteria-free zones that resulted in $CaCO_3$ precipitation in both bacteria-inclusive and bacteria-free zones indicating mineralogy and morphology was not controlled by cell surfaces. Zones containing bacterial cells featured larger crystals compared to bacteria-free zones, and precipitation in both cellular and acellular compartments was attributed to identical bulk solution chemistries (Mitchell and Ferris 2006, Zhang et al. 2018). Based on our real-time monitoring, we have observed a higher abundance of crystals forming in cell-free configurations as opposed to those where cells serve as nucleation sites in the early stages of the MICP process.

Outlook

Confocal microscopy provided significant information, which cannot be observed through traditional material characterization methods. However, the current method also has limitations, as this method to visualize $CaCO_3$ can only be performed for a maximum of 2 h. After this time, $CaCO_3$ in the form of dendrites will form (Supplementary Fig. S4 and Videos S3, S4, and S5). The formation of dendrites obstructed the field of view and obscured the visualization of $CaCO_3$ formed from MICP processes when using brightfield confocal microscopy. Dendrites can be composed of either aragonite and calcite and are formed independently of microbial processes (Jones 2017). To prevent dendrite formation after 2 h, alterations to the methods employed will be required. This may involve methods to minimize evaporation from the samples, which may be the cause of dendrite formation.

Despite the evidence from this paper of the $CaCO_3$ morphology and precipitation rate changes in response to additives, it must be considered that several other factors also have an impact on this process. These can include reactant concentration (Somani et al. 2006, Yao et al. 2009, Nan et al. 2010), temperature (Chong et al. 2014), bacteria concentration and species (Nawarathna et al. 2018a, b), as well as a variety of other additives not investigated during this study (Liendo et al. 2022). Additive experiments from this study were performed under a single set of conditions to reduce the number of variables that could affect the experimentation. $CaCO_3$ morphology and precipitation rate may change substantially if these other factors were to be altered; however, this was beyond the scope of this study.

From the results of this work, several areas of future work can be identified. Different concentrations of additives could be used to further understand the impact of additives on $CaCO_3$ morphology and precipitation rate. Furthermore, use of different bacteria concentrations would help to elucidate the role of bacteria as nucleation sites for $CaCO_3$ precipitation.

Conclusion

Overall, the study demonstrated that $CaCO_3$ precipitation rate and morphology in MICP processes with *S. pasteurii* can be controlled by the inclusion of (in)organic additives. The additives investigated during this work were BSA, BslA, $MgCl_2$, and poly-L-lysine. Our findings indicate that in the presence of additives, there was an increased production of $CaCO_3$ crystals at 100 min compared to the reaction without additives. The incorporation of BslA resulted in larger crystals than reactions containing other additives, including $MgCl_2$. BSA induced a significant number of crystals from the early stages of the reaction (20 min) but did not exert a substantial impact on crystal size compared to conditions without additives. All additives led to a higher content of calcite compared to vaterite after a 24-h reaction, except for $MgCl_2$, which produced a significant quantity of magnesium calcite. Different morphologies can be advantageous for different applications that include papermaking, drug delivery, and teeth whitening products. Different precipitation rates can also be advantageous, e.g. it would be beneficial to have faster MICP rates in self-healing concrete. Future work should direct attention to understanding $CaCO_3$ morphology and rate changes at a range of additive concentrations, as well as under different baseline conditions, so that precise control of $CaCO_3$ precipitation can be achieved. Further understanding of the process of inducing and controlling $CaCO_3$ mineral formation, including precipitation rate, crystal morphology, and/or crystal size, will be essential for the development of novel biologically mediated materials.

Acknowledgements

We thank Dr Gerrit Hilgen for assistance with confocal microscopy techniques and Dr Pietro Maiello for assistance with SEM/EDS/XRD techniques. No specific approval was required for this study.

Supplementary data

Supplementary data is available at *JAMBIO Journal* online.

Conflict of interest : None declared.

Funding

This work was funded by the Research England E3 scheme (2019) and Engineering and Physical Sciences Research Council through Design the Future scheme (EP/R003629/1 and EP/R003777/1).

Author contributions

Jamie Haystead (Data curation, Formal analysis, Methodology, Validation, Visualization, Writing – original draft), Katie Gilmour (Methodology, Investigation, Resources, Writing – review & editing), Angela Sherry (Investigation, Methodology, Supervision, Writing – review & editing), Martyn Dade-Robertson (Conceptualization, Funding acquisition, Resources, Supervision, Visualization, Writing – review & editing), and Meng Zhang (Conceptualization, Funding acquisition, Investigation, Methodology, Project administration, Resources, Supervision, Writing – review & editing)

Data availability

All data supporting this study are provided as supplementary information accompanying this paper at *JAMBIO Journal* online.

References

Abdel Gawwad HA, Mohamed SAE-A, Mohammed SA. Impact of magnesium chloride on the mechanical properties of innovative biomortar. *Mater Lett* 2016;**178**:39–43. https://doi.org/10.1016/j.matlet.2016.04.190.

Achal V, Pan X. Influence of calcium sources on microbially induced calcium carbonate precipitation by *Bacillus* sp. CR2. *Appl Biochem Biotechnol* 2014;**173**:307–17. https://doi.org/10.1007/s12010-014-0842-1.

Ahn JH, Choi KS, Kim H *et al*. Synthesis of aragonite by the carbonation process using stainless refining dust in iron & steel plants. In: Massacci P (ed.), *Developments in Mineral Processing*, Vol. **13**. Rome: Elsevier, 2000, C6–29-35.

Almajed A, Tirkolaei HK, Kavazanjian E *et al*. Enzyme induced biocementated sand with high strength at low carbonate content. *Sci Rep* 2019;**9**:1135. https://doi.org/10.1038/s41598-018-38361-1.

Bachmeier KL, Williams AE, Warmington JR *et al*. Urease activity in microbiologically-induced calcite precipitation. *J Biotechnol* 2002;**93**:171–81. https://doi.org/10.1016/s0168-1656(01)00393-5.

Bahrom H, Goncharenko AA, Fatkhutdinova LI *et al*. Controllable synthesis of calcium carbonate with different geometry: comprehensive analysis of particle formation, cellular uptake, and biocompatibility. *ACS Sustain Chem Eng* 2019;**7**:19142–56. https://doi.org/10.1021/acssuschemeng.9b05128.

Bang SS, Lippert JJ, Yerra U *et al*. Microbial calcite, a bio-based smart nanomaterial in concrete remediation. *Int J Smart Nano Mater* 2010;**1**:28–39. https://doi.org/10.1080/19475411003593451.

Berner RA. The role of magnesium in the crystal growth of calcite and aragonite from sea water. *Geochim Cosmochim Acta* 1975;**39**:489–504. https://doi.org/10.1016/0016-7037(75)90102-7.

Boulos RA, Zhang F, Tjandra ES *et al*. Spinning up the polymorphs of calcium carbonate. *Sci Rep* 2014;**4**:3616. https://doi.org/10.1038/srep03616.

Boyd V, Yoon H, Zhang C *et al*. Influence of Mg^{2+} on $CaCO_3$ precipitation during subsurface reactive transport in a homogeneous silicon-etched pore network. *Geochim Cosmochim Acta* 2014;**135**:321–35. https://doi.org/10.1016/j.gca.2014.03.018.

Boyd VH. *The effect of calcium and magnesium on carbonate miberal precipitation during reactive transport in a model subsurface pore structure*. MSc Thesis, University of Illinois, 2012.

Chang R, Kim S, Lee S *et al*. Calcium carbonate precipitation for CO_2 storage and utilization: a review of the carbonate crystallization and polymorphism. *Front Energy Res* 2017;**5**:17. https://doi.org/10.3389/fenrg.2017.00017.

Chen P-C, Tai CY, Lee KC. Morphology and growth rate of calcium carbonate crystals in a gas–liquid–solid reactive crystallizer. *Chem Eng Sci* 1997;**52**:4171–7. https://doi.org/10.1016/S0009-2509(97)00259-5.

Cheng L, Shahin MA, Mujah D. Influence of key environmental conditions on microbially induced cementation for soil stabilization. *J Geotech Geoenviron Eng* 2017;**143**. https://doi.org/10.1061/(ASCE)GT.1943-5606.0001586.No

Chipman D, Barak Z, Schloss JV. Biosynthesis of 2-aceto-2-hydroxy acids: acetolactate synthases and acetohydroxyacid synthases. *Biochim Biophys Acta* 1998;**1385**:401–19. https://doi.org/10.1016/S0167-4838(98)00083-1.

Chong K-Y, Chia C-H, Zakaria S. Polymorphs calcium carbonate on temperature reaction. *AIP Conf Proc* 2014;**1614**:52–6. .

Clarà Saracho A, Lucherini L, Hirsch M *et al*. Controlling the calcium carbonate microstructure of engineered living building materials. *J Mater Chem A* 2021;**9**:24438–51. https://doi.org/10.1039/D1TA03990C.

Connolly J, Kaufman M, Rothman A *et al*. Construction of two ureolytic model organisms for the study of microbially induced calcium carbonate precipitation. *J Microbiol Methods* 2013;**94**:290–9. https://doi.org/10.1016/j.mimet.2013.06.028.

Dade-Robertson M, Ramirez Figueroa C, Zhang M. Material ecologies for synthetic biology: biomineralization and the state space of design. *Comput Aided Des* 2015;**60**:28–39. https://doi.org/10.1016/j.cad.2014.02.012.

Decho AW, Gutierrez T. Microbial extracellular polymeric substances (EPSs) in ocean systems. *Front Microbiol* 2017;**8**:922. https://doi.org/10.3389/fmicb.2017.00922.

Dhami NK, Alsubhi WR, Watkin E *et al*. Bacterial community dynamics and biocement formation during stimulation and augmentation: implications for soil consolidation. *Front Microbiol* 2017;**8**:1267. https://doi.org/10.3389/fmicb.2017.01267.

Dhami NK, Reddy MS, Mukherjee A. Biomineralization of calcium carbonate polymorphs by the bacterial strains isolated from calcareous sites. *J Microbiol Biotechnol* 2013;**23**:707–14. https://doi.org/10.4014/jmb.1212.11087.

Druzhbin D, Rashchenko SV, Shatskiy A *et al*. New high-pressure and high-temperature CaCO3 polymorph. *ACS Earth Space Chem* 2022;**6**:1506–13. https://doi.org/10.1021/acsearthspacechem.2c00019.

Džakula B, Brečević L, Falini G *et al*. Kinetic approach to biomineralization: interactions of synthetic polypeptides with calcium carbonate polymorphs. *Croat Chem* 2011;**84**:301–14. https://doi.org/10.5562/cca1809.

Fu T, Saracho AC, Haigh SK. Microbially induced carbonate precipitation (MICP) for soil strengthening: a comprehensive review. *Biogeotechnics* 2023;**1**:100002. https://doi.org/10.1016/j.bgtech.2023.100002.

Geyssant J. Features and characteristics of calcium carbonate. In: Tegethoff FW (ed.), *Calcium Carbonate: from the Cretaceous Period into the 21st Century*. Basel: Birkhäuser, 2001, 2–15.

Gómez-Morales J, Torrent-Burgués J, López-Macipe A *et al*. Precipitation of calcium carbonate from solutions with varying Ca^{2+} carbonate ratios. *J Cryst Growth* 1996a;**166**:1020–6. https://doi.org/10.1016/0022-0248(96)00083-8.

Gómez-Morales J, Torrent-Burgués J, Rodríguez-Clemente R. Nucleation of calcium carbonate at different initial pH conditions. *J Cryst Growth* 1996b;**169**:331–8. https://doi.org/10.1016/S0022-0248(96)00381-8.

Haystead JD. *The investigation of microbial induced calcium carbonate precipitation for soil improvement*. Doctoral Thesis, Northumbria University, 2023.

Hirayama K, Akashi S, Furuya M *et al*. Rapid confirmation and revision of the primary structure of bovine serum albumin by ESIMS and frit-FAB LC/MS. *Biochem Biophys Res Commun* 1990;**173**:639–46. https://doi.org/10.1016/S0006-291X(05)80083-X.

Hobley L, Ostrowski A, Rao FV *et al*. BslA is a self-assembling bacterial hydrophobin that coats the *Bacillus subtilis* biofilm. *Proc Natl Acad Sci USA* 2013;**110**:13600–5. https://doi.org/10.1073/pnas.1306390110.

Hu Q, Zhang J, Teng H *et al*. Growth process and crystallographic properties of ammonia-induced vaterite. *Am Mineral* 2012;**97**:1437–45. https://doi.org/10.2138/am.2012.3983.

Huang X, Wang S, Fu L *et al*. Characterization of extracellular polymeric substances by microscopic imaging techniques in wastewater biotreatment: a review. *Environ Eng Sci* 2022;**39**:493–511. https://doi.org/10.1089/ees.2021.0199.

Jiang M, Cao Y, Guo Z-F *et al*. Menaquinone biosynthesis in *Escherichia coli*: identification of 2-succinyl-5-enolpyruvyl-6-hydroxy-3-cyclohexene-1-carboxylate as a novel intermediate and re-evaluation of MenD activity. *Biochemistry* 2007;**46**:10979–89. https://doi.org/10.1021/bi700810x.

Jones B. Review of aragonite and calcite crystal morphogenesis in thermal spring systems. *Sediment Geol* 2017;**354**:9–23. https://doi.org/10.1016/j.sedgeo.2017.03.012.

Liang L, Heveran C, Liu R *et al*. Rational control of calcium carbonate precipitation by engineered *Escherichia coli*. *ACS Synth Biol* 2018;**7**:2497–506. https://doi.org/10.1021/acssynbio.8b00194.

Liendo F, Arduino M, Deorsola FA *et al*. Factors controlling and influencing polymorphism, morphology and size of calcium carbonate synthesized through the carbonation route: a review. *Powder Technol* 2022;**398**:117050. https://doi.org/10.1016/j.powtec.2021.117050.

Lv C, Tang C-S, Zhang J-Z *et al*. Effects of calcium sources and magnesium ions on the mechanical behavior of MICP-treated calcareous sand: experimental evidence and precipitated crystal insights. *Acta Geotech* 2022;**18**:2703–17. https://doi.org/10.1007/s11440-022-01748-6.

Mann S. *Biomineralization: Principles and Concepts in Bioinorganic Materials Chemistry*. Oxford: Oxford University Press, 2001.

Minkowicz L, Dagan A, Uvarov V *et al*. Controlling calcium carbonate particle morphology, size, and molecular order using silicate. *Materials* 2021;**14**:3525. https://doi.org/10.3390/ma14133525.

Mitchell AC, Ferris FG. The influence of *Bacillus pasteurii* on the nucleation and growth of calcium carbonate. *Geomicrobiol J* 2006;**23**:213–26. https://doi.org/10.1080/01490450600724233.

Morris RJ, Schor M, Gillespie RMC *et al*. Natural variations in the biofilm-associated protein BslA from the genus *Bacillus*. *Sci Rep* 2017;**7**:6730. https://doi.org/10.1038/s41598-017-06786-9.

Nan Z, Yang Q, Chen Z. Novel morphologies and phase transformation of $CaCO_3$ crystals formed in CDS and urea aqueous solution. *J Cryst Growth* 2010;**312**:705–13. https://doi.org/10.1016/j.jcrysgro.2009.12.044.

Nawarathna THK, Nakashima K, Fujita M *et al*. Effects of cationic polypeptide on $CaCO_3$ crystallization and sand solidification by microbial-induced carbonate precipitation. *ACS Sustain Chem Eng* 2018a;**6**:10315–22. https://doi.org/10.1021/acssuschemeng.8b01658.

Nawarathna THK, Nakashima K, Kawasaki S. Enhancement of microbially induced carbonate precipitation using organic biopolymer. *Int J GEOMATE* 2018b;**14**:7–12. https://doi.org/10.21660/2018.41.7223.

Niu Y-Q, Liu J-H, Aymonier C *et al*. Calcium carbonate: controlled synthesis, surface functionalization, and nanostructured materials. *Chem Soc Rev* 2022;**51**:7883–943. https://doi.org/10.1039/D1CS00519G.

Putra H, Yasuhara H, Kinoshita N *et al*. Effect of magnesium as substitute material in enzyme-mediated calcite precipitation for soil-improvement technique. *Front Bioeng Biotechnol* 2016;**4**:37. https://doi.org/10.3389/fbioe.2016.00037.

Ramos R, Bernard J, Ganachaud F *et al*. Protein-based encapsulation strategies: toward micro- and nanoscale carriers with increased functionality. *Small Sci* 2022;**2**:2100095. https://doi.org/10.1002/smsc.202100095.

Roberts AD, Finnigan W, Kelly PP *et al*. Non-covalent protein-based adhesives for transparent substrates—bovine serum albumin vs. recombinant spider silk. *Mater Today Bio* 2020;**7**:100068. https://doi.org/10.1016/j.mtbio.2020.100068.

Roberts AD, Whittall D, Breitling R *et al*. Blood, sweat and tears: extraterrestrial regolith biocomposites with in vivo binders. *Mater Today Bio* 2021;**12**:100136. http://doi.org/10/1016/j.mtbio.2021.100136

Robles-Fernández A, Areias C, Daffonchio D *et al*. The role of microorganisms in the nucleation of carbonates, environmental implications and applications. *Minerals* 2022;**12**:1562. https://doi.org/10.3390/min12121562.

Rowshanbakht K, Khamehchiyan M, Sajedi RH *et al*. Effect of injected bacterial suspension volume and relative density on carbonate precipitation resulting from microbial treatment. *Ecol Eng* 2016;**89**:49–55. https://doi.org/10.1016/j.ecoleng.2016.01.010.

Somani RS, Patel KS, Mehta AR *et al*. Examination of the polymorphs and particle size of calcium carbonate precipitated using still effluent (i.e., $CaCl_2$ + NaCl solution) of soda ash manufacturing process. *Ind Eng Chem Res* 2006;**45**:5223–30. https://doi.org/10.1021/ie0513447.

Tang G, Jia C, Wang G *et al*. Role of Na-montmorillonite on microbially induced calcium carbonate precipitation. *Molecules* 2021;**26**:6211. https://doi.org/10.3390/molecules26206211.

Udrea I, Capat C, Olaru EA *et al*. Vaterite synthesis via gas–liquid route under controlled pH conditions. *Ind Eng Chem Res* 2012;**51**:8185–93. https://doi.org/10.1021/ie202221m.

Van Paassen LA. *Biogrout (ground improvement by microbially induced carbonate precipitation)*. Doctoral Thesis, Delft University of Technology, 2009.

Whiffin VS. *Microbial $CaCO_3$ precipitation for the production of biocement*. Doctoral Thesis, Murdoch University, 2004.

Wiley WR, Stokes JL. Effect of pH and ammonium ions on the permeability of *Bacillus pasteurii*. *J Bacteriol* 1963;**86**:1152–6. https://doi.org/10.1128/jb.86.6.1152-1156.1963.

Wu S, Chiang C-Y, Zhou W. Formation mechanism of CaCO3 spherulites in the myostracum layer of limpet shells. *Cryst* 2017;**7**:319. https://doi.org/10.3390/cryst7100319.

Xiao Y, Ma G, Wu H *et al*. Rainfall-induced erosion of biocemented graded slopes. *Int J Geomech* 2022;**22**: 1. https://doi.org/10.1061/(ASCE)GM.1943-5622.0002239.

Xu J, Du Y, Jiang Z *et al*. Effects of calcium source on biochemical properties of microbial CaCO(3) precipitation. *Front Microbiol* 2015;**6**:1366. https://doi.org/10.3389/fmicb.2015.01366.

Xu XC, Guo HX, Cheng XH *et al*. The promotion of magnesium ions on aragonite precipitation in MICP process. *Constr Build Mater* 2020;**263**:1–9. https://doi.org/10.1016/j.conbuildmat.2020.120057.

Yao Y, Dong W, Zhu S *et al*. Novel morphology of calcium carbonate controlled by poly(l-lysine). *Langmuir* 2009;**25**:13238–43. https://doi.org/10.1021/la901913d.

Yasushi K. A study of the polymorphic formation of calcium carbonate in thermal springs with an emphasis on the effect of temperature. *Bull Chem Soc Jpn* 1962;**35**:1980–5. https://doi.org/10.1246/bcsj.35.1980.

Yi D, Zhang H, Zhang W *et al*. Fabrication of patterned calcium carbonate materials through template-assisted microbially induced calcium carbonate precipitation. *RSC Adv* 2021;**11**:28643–50. https://doi.org/10.1039/D1RA04072C.

Yoon JH, Lee KC, Weiss N *et al*. *Sporosarcina aquimarina* sp. nov., a bacterium isolated from seawater in Korea, and transfer of *Bacillus globisporus* (Larkin and Stokes 1967), *Bacillus psychrophilus* (Nakamura 1984) and *Bacillus pasteurii* (Chester 1898) to the genus *Sporosarcina* as *Sporosarcina globispora* comb. nov., *Sporosarcina psychrophila* comb. nov. and *Sporosarcina pasteurii* comb. nov., and emended description of the genus *Sporosarcina*. *Int J Syst Evol Microbiol* 2001;**51**:1079–86. https://doi.org/10.1099/00207713-51-3-1079.

Yu X, Chu J, Wu S *et al*. Production of biocement using steel slag. *Constr Build Mater* 2023;**383**:131365. https://doi.org/10.1016/j.conbuildmat.2023.131365.

Yu X, Pan X. One-phase improvement of sandy soil using seawater-based soybean-induced carbonate precipitation. *J Sustainable Cem-Based Mater* 2023;**12**:962–71. https://doi.org/10.1080/21650373.2022.2142985.

Yu X, Rong H. Seawater based MICP cements two/one-phase cemented sand blocks. *Appl Ocean Res* 2022;**118**:102972. https://doi.org/10.1016/j.apor.2021.102972.

Yu X, Yang H, Wang H. A cleaner biocementation method of soil via microbially induced struvite precipitation: a experimental and numerical analysis. *J Environ Manage* 2022;**316**:115280. https://doi.org/10.1016/j.jenvman.2022.115280.

Yu X, Zhang Q. Microbially/CO_2-derived $CaCO_3$ cement and its microstructural and mechanical performance. *J Sustainable Cem-Based Mater* 2023a;**12**:1156–68. https://doi.org/10.1080/21650373.2023.2178539.

Yu X, Zhang Z. Calcium carbide sludge activated fly ash mixture for offshore construction and its crack repair using seawater-mixed bioslurry cement. *J Clean Prod* 2023b;**395**:136456. https://doi.org/10.1016/j.jclepro.2023.136456.

Zaerkabeh R, Sadeghi AM, Afshin H *et al*. Crack healing and mechanical properties of bacteria-based self-healing cement mortar. *Period Polytech Civ Eng* 2022;**66**:581–92. https://doi.org/10.3311/PPci.18803.

Zhang W, Ju Y, Zong Y *et al*. In situ real-time study on dynamics of microbially induced calcium carbonate precipitation at a single-cell level. *Environ Sci Technol* 2018;**52**:9266–76. https://doi.org/10.1021/acs.est.8b02660.

Received 7 October 2023; **revised** 28 November 2023; **accepted** 15 December 2023